Compressibility of synthetic Mg-Al tourmalines to 60 GPa

ELEANOR J. BERRYMAN[1],*, DONGZHOU ZHANG[2], BERND WUNDER[3], AND THOMAS S. DUFFY[1]

[1]Department of Geosciences, Princeton University, Princeton, New Jersey 08544, U.S.A.
[2]Hawai'i Institute of Geophysics and Planetology, University of Hawai'i at Manoa, Honolulu, Hawai'i 96822, U.S.A. Orcid 0000-0002-6679-892X
[3]Chemistry and Physics of Earth Materials, GFZ German Research Centre for Geosciences, 14473 Potsdam, Germany

ABSTRACT

High-pressure single-crystal X-ray diffraction patterns on five synthetic Mg-Al tourmalines with near end-member compositions [dravite $NaMg_3Al_6Si_6O_{18}(BO_3)_3(OH)_3OH$, K-dravite $KMg_3Al_6Si_6O_{18}(OH)_3OH$, magnesio-foitite $\square(Mg_2Al)Al_6Si_6O_{18}(BO_3)_3(OH)_3OH$, oxy-uvite $CaMg_3Al_6Si_6O_{18}(BO_3)_3(OH)_3O$, and olenite $NaAl_3Al_6Si_6O_{18}(BO_3)_3O_3OH$, where $\square$ represents an *X*-site vacancy] were collected to 60 GPa at 300 K using a diamond-anvil cell and synchrotron radiation. No phase transitions were observed for any of the investigated compositions. The refined unit-cell parameters were used to constrain third-order Birch-Murnaghan pressure-volume equation of states with the following isothermal bulk moduli (K_0 in GPa) and corresponding pressure derivatives ($K_0' = \partial K_0/\partial P)_T$: dravite $K_0 = 97(6)$, $K_0' = 5.0(5)$; K-dravite $K_0 = 109(4)$, $K_0' = 4.3(2)$; oxy-uvite $K_0 = 110(2)$, $K_0' = 4.1(1)$; magnesio-foitite $K_0 = 116(2)$, $K_0' = 3.5(1)$; olenite $K_0 = 116(6)$, $K_0' = 4.7(4)$. Each tourmaline exhibits highly anisotropic behavior under compression, with the **c** axis 2.8–3.6 times more compressible than the **a** axis at ambient conditions. This anisotropy decreases strongly with increasing pressure and the **c** axis is only ~14% more compressible than the **a** axis near 60 GPa. The octahedral *Y*- and *Z*-sites' composition exerts a primary control on tourmaline's compressibility, whereby Al content is correlated with a decrease in the **c**-axis compressibility and a corresponding increase in K_0 and K_0'. Contrary to expectations, the identity of the *X*-site-occupying ion (Na, K, or Ca) does not have a demonstrable effect on tourmaline's compression curve. The presence of a fully vacant *X* site in magnesio-foitite results in a decrease of K_0' relative to the alkali and Ca tourmalines. The decrease in K_0' for magnesio-foitite is accounted for by an increase in compressibility along the **a** axis at high pressure, reflecting increased compression of tourmaline's ring structure in the presence of a vacant *X* site. This study highlights the utility of synthetic crystals in untangling the effect of composition on tourmaline's compression behavior.

Keywords: Tourmaline, synthetic, single-crystal X-ray diffraction, equation of state, diamond-anvil cell

INTRODUCTION

Tourmaline is the most common borosilicate and is found in various rock-forming environments throughout the crust (van Hinsberg et al. 2011). This supergroup mineral comprises at least 33 end-member species represented by the general structural formula $XY_3Z_6T_6O_{18}(BO_3)_3V_3W$. Tourmaline's complex crystal chemistry allows its structure to incorporate at least 26 elements of varying size and charge (Bosi 2018). Of these, the current end-member-defining site-occupants are Na, Ca, K, and vacancy ($\square$) at the ninefold-coordinated *X* site; Mg, Fe^{2+}, Fe^{3+}, Al, Li, Mn, Cr, V at the octahedral *Y* and *Z* sites; Si and Al at the tetrahedral *T* site; OH and O at the *V* site; and OH, O, and F at the *W* site. The B site is the only cation site that does not exhibit solid solution. However, B is not limited to the B site. In both natural and synthetic Al-rich tourmalines, significant amounts of excess B (<2.3 pfu) have been reported to occur at the *T* site

(e.g., Tagg et al. 1999; Hughes et al. 2000, 2001; Schreyer et al. 2000, 2002; Marler et al. 2002; Marschall et al. 2004; Ertl et al. 2012a; Kutzschbach et al. 2016).

Tourmaline's stability throughout the crust and possibly the uppermost mantle is surprising in view of the expectation that the presence of multiple coordination environments in its structure might limit tourmaline's stability (Bosi 2018). At ambient pressure, tourmaline has been experimentally shown to be stable from 150 K until it dehydrates at 1200–1280 K and is then reported to break down to products including cordierite at 1400 K (Hemingway et al. 1996). Upon compression, single-crystal X-ray diffraction (XRD) up to 23.6 GPa supported by luminescence spectroscopy suggests dravitic tourmaline undergoes a subtle second-order phase transition from rhombohedral *R*3*m* to *R*3 symmetry at 15 GPa (O'Bannon et al. 2018). Luminescence spectroscopy at higher pressure shows the latter structure remains (meta)stable to at least ~65 GPa (O'Bannon et al. 2018). Dravitic tourmaline has been synthesized up to 6–8 GPa, <1000 °C, above which it decomposes to several Mg-Al phases (Krosse 1995). The upper limit of tourmaline's stability is reduced in a Si-saturated

system, and Mg-Al tourmaline has been shown experimentally to decompose around 4.5–5 GPa and 700 °C (Ota et al. 2008).

Tourmaline's complex chemistry and crystal properties historically distinguished it as a mineral of scientific interest (Dutrow and Henry 2011). The occurrence of striking concentric and sector zoning within single crystals results from the low intra-volume diffusion of elements in its structure even at high temperature (Henry and Dutrow 1996). Combined with its resistance to mechanical and chemical weathering, tourmaline's compositional zoning underlies its traditional application as a sediment provenance indicator (e.g., Henry and Dutrow 1992). More recently, efforts are being made to decode tourmaline's record of its host rock's evolution through pressure, temperature, and compositional space. To fully unlock tourmaline's potential as a petrogenetic indicator mineral (e.g., Henry and Guidotti 1985; van Hinsberg et al. 2011), an understanding of its endmember thermodynamic parameters and crystal chemistry at high pressure and temperature is needed.

Current knowledge of the elastic properties of tourmaline is limited to a few ultrasonic elasticity studies on natural samples at ambient conditions (Helme and King 1978; Tatli and Özkan 1987; Pandey and Schreuer 2012) and high-pressure powder and single-crystal XRD (up to 27.8 GPa, Li et al. 2004; 18 GPa, Xu et al. 2016; 23.6 GPa, O'Bannon et al. 2018). The reported ambient isothermal bulk moduli (K_0) and their pressure derivatives [$K_0' = (\partial K_0/\partial P)_T$] show considerable scatter (Table 1), which has been proposed to reflect compositional variability of the investigated samples (Helme and King 1978). Composition, especially Al content, is known to strongly influence tourmaline's long-range crystal structure through variation of its unit-cell parameters (Bosi et al. 2010). It is therefore likely that composition may influence tourmaline's other properties, such as its behavior under compression. The Fe content of tourmaline has been correlated with variations in some of the single-crystal elastic constants, however the investigated compositional range and corresponding elastic variability were limited (Pandey and Schreuer 2012). Similar to other cyclosilicates, such as beryl and cordierite,

tourmaline is known to have strongly anisotropic compressibility, whereby the **c** axis perpendicular to the ring structure is more compressible than the **a** axis. Due to the size and location of the highly compressible X site directly above the ring structure in the **c** direction (Fig. 1), it has been hypothesized that the X site may exert a primary control on tourmaline's compressibility, especially along **c** (e.g., Xu et al. 2016; O'Bannon et al. 2018).

Synthetic crystals provide an optimal means to explore the relative effects of pressure, temperature, and fluid composition on the incorporation of elements in tourmaline (von Goerne et
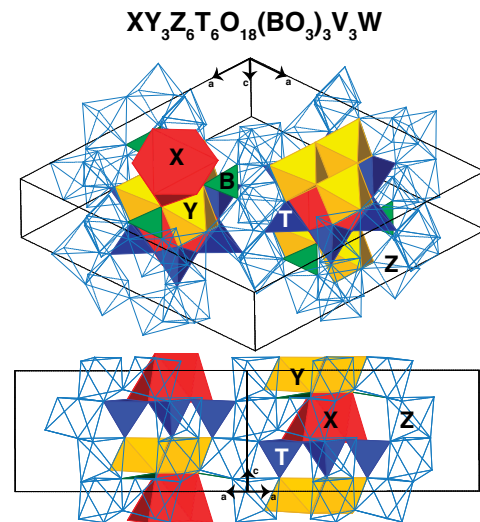
$$XY_3Z_6T_6O_{18}(BO_3)_3V_3W$$

FIGURE 1. Tourmaline's crystal structure and unit cell viewed in two orientations. The ninefold-coordinated X site (red) is coordinated below to the six-membered ring of tetrahedral T sites (blue) and above to the trigonal B site (green) and the octahedral Y site (yellow) trimer. The octahedral Z site (transparent with blue frame) forms a network around the other sites and is connected in the c direction in 3_1 chains. The V and W anion sites are not identified in this figure. (Color online.)

TABLE 1. Tourmaline equation of state parameters

	K_0 (GPa)	K_0'	V_0 (Å³)	K_0 (GPa)	K_0'	V_0 (Å³)	
Synthetic tourmaline							
Dravite	97(6)	5.0(5)	1556(4)	110(2)	[4]	1551(3)	This study
K-dravite	109(4)	4.3(2)	1567(3)	115(1)	[4]	1564(2)	
Oxy-uvite	110(2)	4.1(1)	1573(2)	112.5(6)	[4]	1571(1)	
Magnesio-foitite	116(2)	3.5(1)	1560(2)	105.8(9)	[4]	1568(2)	
Olenite	116(6)	4.7(4)	1490(4)	128(2)	[4]	1485(3)	
Natural tourmaline							
Dravite	110(3)	4.6(8)	1578.2(2)	112(1)	[4]	1578.2(2)	O'Bannon et al. (2018)
Uvite	97(1)	12.4(4)	1537(1)	120(2)	[4]	1537(1)	Xu et al. (2012)
Elbaite-schorl	119[a]		1542				Pandy and Schreuer (2012)
Elbaite-schorl	118[a]		1542				
Elbaite-schorl	117[a]		1568				
Schorl-dravite	116[a]		1578				
Schorl-dravite	118[a]		1578				
Schorl	120[a]		1553				Tatli and Özkan (1987)
Elbaite	115[a]		1555				
Elbaite	114[a]		1545				
Elbaite	115[a]		1542				
Uvite	115[a]		1586				
Schorl-elbaite	121[a]		1550				Helme and King (1978)

Note: Brackets indicate the value was fixed during fitting.
[a] Isothermal bulk moduli calculated from isentropic bulk moduli using the volume thermal expansivity of Pandey and Schreuer (2012) and the constant-pressure specific heat of Ogorodova et al. (2004).

al. 2011; Berryman et al. 2014, 2015, 2016a; Kutzschbach et al. 2017). Moreover, the characterization of synthetic crystals has provided valuable insight into tourmaline's chemical flexibility and how composition affects tourmaline's long- and short-range crystal structure (Ertl et al. 2003; London et al. 2006; Setkova et al. 2009, 2017; Wunder et al. 2015; Berryman et al. 2016b). Whereas natural tourmaline crystals represent complex solid solutions of multiple end-members and contain significant amounts of minor elements, synthetic crystals can be grown with restricted compositions, allowing for more direct determination of the chemical control on physical properties.

High-pressure XRD experiments on minerals constrain their stability and their pressure-volume equation of state (P-V EoS). Moreover, studies on minerals of varying composition provide valuable information on the effect of chemistry on these mineral properties (e.g., Zhang 1998; Zhang et al. 1999; Boffa Ballaran et al. 2012; Xu et al. 2019). Here, a collection of synthetic Mg-Al tourmaline (dravite, K-dravite, magnesio-foitite, oxy-uvite, and olenite) is used to constrain the 300-K P-V EoS of five tourmalines with distinct X-site occupancies (Na, K, Ca, and vacancies) and Mg-Al contents to 60 GPa.

EXPERIMENTAL METHODS

Synthetic samples

The magnesio-foitite and oxy-uvite samples were synthesized by Berryman et al. (2016b) and the olenite sample by Kutzschbach et al. (2016). Information on the synthesis and characterization [electron microprobe analysis (EMPA), powder and single-crystal X-ray diffraction (XRD), and Raman spectroscopy] is available in Berryman et al. (2016b) for magnesio-foitite (sample MF2) and oxy-uvite (sample CN11), and in Kutzschbach et al. (2016) for olenite (columnar crystals; MK1). The dravite (sample 471-1) and K-dravite (sample 471-2) were newly synthesized for this study using a method modified after Berryman et al. (2015). Information on the synthesis and characterization (EMPA, powder, and single-crystal XRD) is available in the Supplementary Material[1].

The five synthetic samples investigated in this study represent four distinct Mg-Al tourmaline species (dravite, K-dravite, oxy-uvite, magnesio-foitite) and the Na-Al tourmaline species, olenite. The compositions of the general cation sites (X, Y, Z, and T) for each of the synthetic tourmaline samples are in Table 2. The theoretical end-member species represented by this collection have the following idealized formulas [$XY_3Z_6T_6O_{18}(BO_3)_3V_3W$]: dravite $NaMg_3Al_6Si_6O_{18}(BO_3)_3(OH)_3OH$, K-dravite $KMg_3Al_6Si_6O_{18}(BO_3)_3(OH)_3OH$, oxy-uvite $CaMg_3Al_6Si_6O_{18}(BO_3)_3(OH)_3O$, magnesio-foitite $\square$ (Mg_2Al) $Al_6Si_6O_{18}(BO_3)_3(OH)_3OH$, and olenite $NaAl_3Al_6Si_6O_{18}(BO_3)_3O_3OH$. The X-site compositions of the Mg-Al tourmalines are distinct, representing each of the principal X-site-occupying ions of the tourmaline supergroup: Na, Ca, vacancy $\square$, and K. Although K most commonly occurs in minor or trace amounts in tourmaline, K-dominant species have been found (e.g., Grice et al. 1993; Shimizu and Ogasawara 2005). There is currently only one K-bearing tourmaline species recognized by the International Mineralogical Association's Commission on New Minerals, Nomenclature and Classification (IMA-CNMNC): maruyamaite $K(MgAl_2)(Al_5Mg)$ $Si_6O_{18}(BO_3)_3(OH)_3O$ (Lussier et al. 2016).

The olenite sample is distinguished from the other samples by the absence of

Mg at the Y and Z sites, which are instead fully occupied by Al. It is important to note that the idealized ordering of Mg and Al between the Y and Z sites present in the theoretical end-member formulas of the Mg-Al tourmalines is never observed in natural or synthetic tourmaline. The large difference in average <Y-O> and <Z-O> bond lengths imposed by such ordering would destabilize tourmaline's structure (Bosi and Lucchesi 2007; Bosi 2018). The Mg-Al tourmalines investigated here therefore show significant Mg-Al disorder between the Y and Z sites. Likely owing to their high Al content, the synthetic magnesio-foitite and olenite contain significant amounts of tetrahedral B: 0.34(4) and 1.4(1) ^TB pfu, respectively (Table 2). In addition, all the synthetic tourmalines have a significant number of X-site vacancies. As a result of their variable short- and long-range crystal structure, the investigated tourmalines span a range of unit-cell volumes observed for natural tourmalines (Fig. 2).

X-ray diffraction

The high-pressure single-crystal XRD patterns were collected using symmetric diamond-anvil cells (DAC) equipped with type 1a diamonds with 300 µm culets mounted on X-ray transparent cBN (upstream) and WC (downstream) seats. A sample chamber was made in a Re gasket indented to a ~30–40 µm thickness using either an electric-discharge machining drill (154 µm hole diameter) or a laser drilling system (200 µm hole diameter). A single tourmaline crystal (~14 × 14 × 80 µm or smaller) was loaded together with a ruby sphere and a piece of powdered gold as pressure standards in each DAC. A neon-gas pressure-transmitting medium was loaded using a gas-loading system (Rivers et al. 2008). High-pressure single-crystal X-ray diffraction patterns were collected up to 60 GPa in <5 GPa pressure steps along with ambient X-ray diffraction patterns at beamline 13BM-C at the GeoSoilEnviroCARS (GSECARS) sector of the Advanced Photon Source. The synchrotron X-ray was monochromated to a wavelength of λ = 0.434 Å (28.6 keV) within a 1 eV bandwidth. The X-ray spot was focused to ~12 (horizontal) ×18 (vertical) µm on the sample and diffraction images were collected on a MAR165 CCD area detector. The sample-detector distance (~155 mm) and detector tilt were calibrated using a NIST LaB$_6$ standard. Angle-dispersive X-ray diffraction data for tourmaline was collected in 1° steps (step scans) across each DAC's downstream opening angle (dravite 27°, K-dravite 37°, oxy-uvite 40°, magnesio-foitite 33°, and olenite 27°). Exposures (10–20 s/°) were collected with the detector in line with the incident X-ray (2θ = 0°). In addition, wide-step exposures across each half of the DAC opening angle were collected with the detector at 2θ = 0° and with the detector rotated 10° around the 2θ axis. A wide scan of X-ray diffraction data from the tourmaline crystal and the powdered gold pressure standard across the entire downstream opening angle of the DAC at one detector position (2θ = 0°) was also collected at each pressure step.

The diffraction quality of the different crystals varied as indicated by the number of sharp single-crystal diffraction spots that were indexed to hexagonal symmetry: oxy-uvite, 142 peaks; magnesio-foitite, 78 peaks; olenite, 68 peaks; dravite, 55 peaks; and K-dravite, 38 peaks. Diffraction spots from each step-scan diffraction pattern were identified and combined using the GSE_ADA/RSV software package (Dera et al. 2013). The unit-cell and orientation matrices were identified with the program CELL_NOW (Bruker AXS Inc.). Refinement of the unit-cell parameters was done using peaks identified in the combined wide-scan diffraction patterns collected at two detector positions.

Gold's powder XRD pattern was integrated using Dioptas (Clemens and Prakapenka 2015) and the unit-cell parameter determined from the position of the (111) diffraction peak. Pressure was determined using the pressure-volume equation of state of Dewaele et al. (2004) and Fei et al. (2007). The neon pressure medium crystallizes at 4.7 GPa (Finger et al. 1981), leading to reduced hydrostatic conditions inside the DAC. The differential stress at each pressure point was estimated using the approach of Singh and Kenichi (2001), which relies on comparing gold's

TABLE 2. Investigated synthetic tourmalines general cation site occupancies [$XY_3Z_6T_6O_{18}(BO_3)_3V_3W$]

	$^{[9]}X$	$^{[6]}Y$	$^{[6]}Z$	$^{[4]}T$
Dravite[a]	0.84(6) **Na**, 0.16(6) $\square$	1.8(6) **Mg**, 1.2(7) Al	5.3(6) **Al**, 0.7(6) Mg	5.6(3) **Si**, 0.1(4) Al, 0.4(2) B
K-dravite[a]	0.5(1) **K**, 0.5(1) $\square$, 0.1(5) Na	1.8(6) **Mg**, 1.3(6) Al	5.4(5) **Al**, 0.6(5) Mg	5.7(2) **Si**, 0.2(2) Al, 0.2(1) B
Oxy-uvite	0.64(1) **Ca**, 0.36(1) $\square$	1.5(1) **Mg**, 1.5(1) Al	4.9(2) **Al**, 1.1(2) Mg	6 **Si**
Magnesio-foitite	0.91(6) $\square$, 0.09(6) Na	1.4(2) **Mg**, 1.6(2) **Al**	4.9(2) **Al**, 1.1(2) Mg	5.66(4) **Si**, 0.34(4) B
Olenite	0.58(1) **Na**, 0.42(1) $\square$	2.83(1) **Al**	6 **Al**	4.6(1) **Si**, 1.4(1) B

Notes: Box indicates vacancy. Brackets indicate coordination number of site. Bold typeface indicates major site-occupying ion. Values for oxy-uvite (sample CN11) and magnesio-foitite (sample MF2) are from Berryman et al. (2016b). Values for olenite (sample MK1, columnar) from Kutzschbach et al. (2016). These studies determined the site occupancies by a combination of EMPA and structure refinement of single-crystal XRD diffraction data.
[a] Site occupancies determined by normalization of EMPA to 18 cations at the Y, Z, and T sites. Mg-Al disorder between Y and Z sites calculated using empirical relationship of Bosi (2018). See supplementary material[1] for additional details.
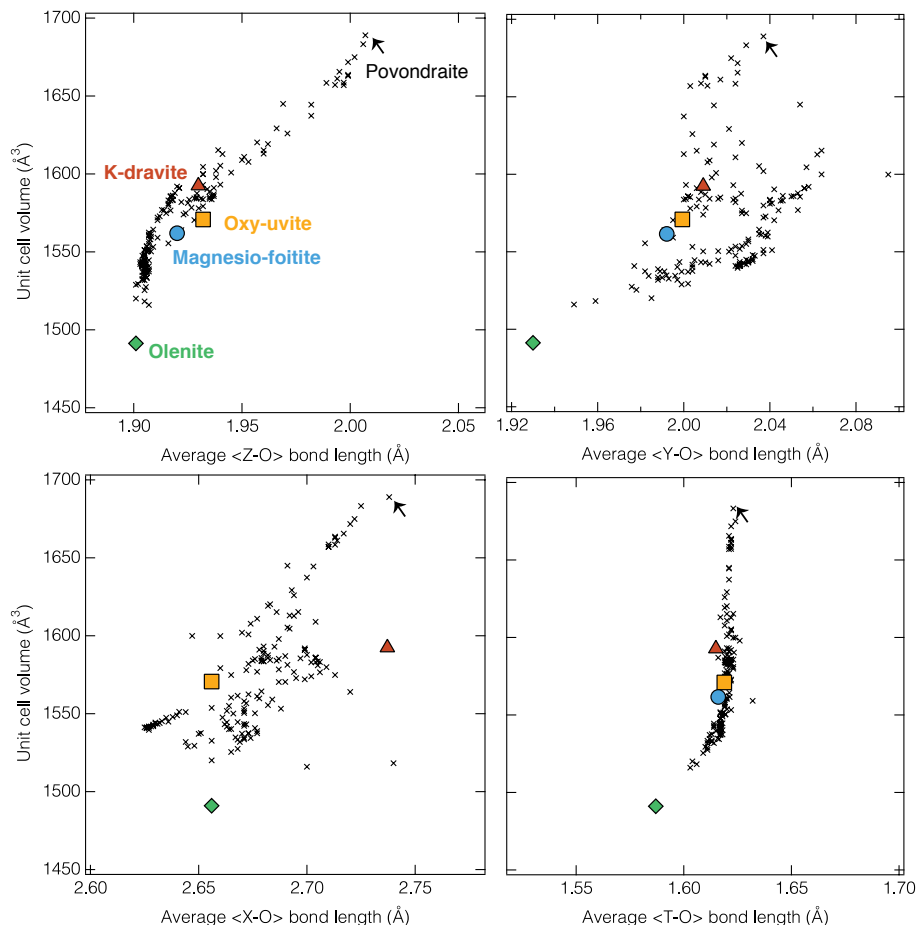
FIGURE 2. Unit-cell volume of synthetic K-dravite (red triangle), oxy-uvite (yellow square), magnesio-foitite (blue circle), and olenite (green diamond), and natural tourmaline (black x) as a function of their average Z-O, Y-O, X-O, and T-O bond lengths. The arrow is pointing to data for natural povondraite (Grice et al. 1993). Values for the other natural tourmalines are from: Ertl et al. (2006, 2007, 2008a, 2008b, 2009, 2010a, 2010b, 2010c, 2012a, 2012b, 2013, 2016a, 2016b), Bosi (2008), Lussier et al. (2008, 2011a, 2011b, 2016), Bosi et al. (2010, 2012, 2013a, 2013b, 2013c, 2014a, 2014b, 2015a, 2015b, 2015c, 2016a, 2016b, 2017a, 2017c), Clark et al. (2011), Filip et al. (2012), Gatta et al. (2012), Cempírek et al. (2013), Bačík et al. (2013, 2015), Novák et al. (2013), Reznitskii et al. (2014), and Grew et al. (2018). Values for the synthetic tourmalines are from Berryman et al. (2016b) and Kutzschbach et al. (2016). (Color online.)

unit-cell parameter based on the (002), (022), and (111) diffraction peaks and the elastic anisotropy factor of Tsuchiya and Kawamura (2002). In all experiments, detectable differential stress appeared at ~10 GPa and increased with pressure, but never exceeded 0.6 GPa.

RESULTS AND DISCUSSION

X-ray diffraction

The unit-cell parameters of the tourmalines at each pressure step are listed in Supplemental[1] Table S1 and presented in Figure 3. The unit-cell parameters were consistently refined to a rhombohedral cell at all investigated pressure points and no phase transformations were identified over the investigated pressure range. O'Bannon et al. (2018) reported a subtle phase transition in dravitic tourmaline at 15 GPa resulting from a change in the distortion behavior of the ring structure under compression. This phase transition changes the space group from $R3m$ to $R3$, reflecting the loss of the mirror plane. This second-order phase transition does not change the topology of the tourmaline struc-

ture and rhombohedral symmetry was maintained. It would not be detectable in our data sets because it is not associated with a change in unit-cell volume.

The pressure and unit-cell volume (P-V) data set for each investigated tourmaline was fit to both second- and third-order Birch-Murnaghan P-V equations of state (P-V EoS) using fully weighted parameters and the EosFit-7c program (Angel et al. 2014; Gonzalez-Platas et al. 2016). The resulting ambient isothermal bulk moduli (K_0) and their respective pressure derivatives (K'_0) are shown in Table 1. The values are in reasonable agreement with previous studies. The ambient unit-cell volume (V_0) constrained by the fit for each composition is in close agreement with those determined for single crystals from the corresponding synthesis experiment: dravite 1556.4(4) Å³; K-dravite 1569.2(3) Å³; oxy-uvite 1570.7(3) Å³; magnesio-foitite 1562.1(4) Å³; olenite 1491.3(2) Å³. The quality of the fits can be further evaluated by considering the fit of the P-V EoS in normalized pressure vs. Eulerian strain space (F_E-f plots in Supplementary Material[1]).
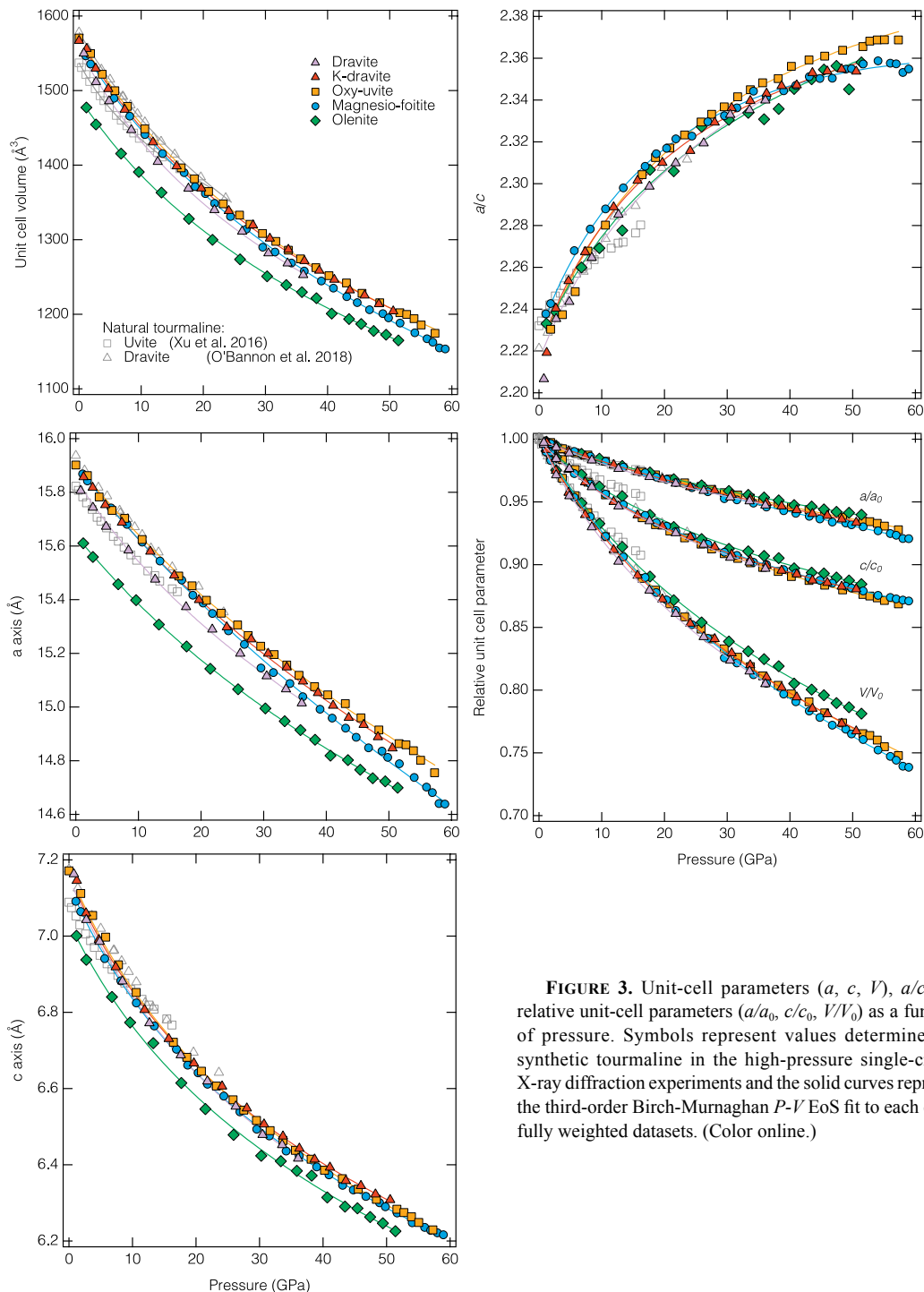
FIGURE 3. Unit-cell parameters (a, c, V), a/c, and relative unit-cell parameters (a/a_0, c/c_0, V/V_0) as a function of pressure. Symbols represent values determined for synthetic tourmaline in the high-pressure single-crystal X-ray diffraction experiments and the solid curves represent the third-order Birch-Murnaghan P-V EoS fit to each of the fully weighted datasets. (Color online.)

In these coordinates, the third-order Birch-Murnaghan P-V EoS is needed to fit the data of all tourmaline compositions, with the exception of synthetic dravite, where the second-order Birch-Murnaghan P-V EoS fits the data equally well.

A parametrized version of the third-order Birch Murnaghan EoS was fit to the weighted axial unit-cell parameters (a and c) as a function of pressure using the EosFit-7c program. The resulting axial moduli (M_{a0} and M_{c0}) were converted to linear compressibilities at ambient conditions (β_{a0} and β_{c0}) following the approach of Angel et al. (2014) (Table 3). The linear compressibility at each pressure step was calculated following the approach of Xia et al. (1998) (Fig. 4). The results confirm tourmaline's highly anisotropic elasticity, whereby the **c** axis is 2.8–3.6 times more compressible than the **a** axis at ambient

TABLE 3. Tourmaline axial compressibility

	β_{a_0} (10^{-3} GPa^{-1})	M_{a_0} (GPa)	M'_{a_0}	a_0 (Å)	β_{c_0} (10^{-3} GPa^{-1})	M_{c_0} (GPa)	M'_{c_0}	c_0 (Å)	
				Synthetic tourmaline					
Dravite	1.98(6)	505(16)	12(1)	15.824(5)	7.1(6)	141(13)	14(1)	7.185(13)	This study
K-dravite	1.83(5)	547(16)	9.7(7)	15.889(6)	6.4(3)	156(8)	14.0(6)	7.181(9)	
Oxy-uvite	1.82(4)	551(13)	9.9(6)	15.907(5)	6.6(2)	151(4)	13.1(2)	7.204(5)	
Magnesio-foitite	1.88(4)	532(12)	8.0(4)	15.907(5)	5.6(1)	179(4)	12.4(2)	7.134(5)	
Olenite	1.83(7)	546(20)	13(1)	15.639(8)	5.1(5)	195(18)	12(1)	7.040(16)	
				Natural tourmaline					
Dravite[a]	2.09(5)	480(11)	16(2)	15.937	5.0(1)	201(4)	10.0(9)	7.1749	O'Bannon et al. (2018)
Uvite[a]	2.4(2)	424(25)	33(8)	15.823(6)	5.4(3)	185(8)	31(4)	7.089(4)	Xu et al. (2012)

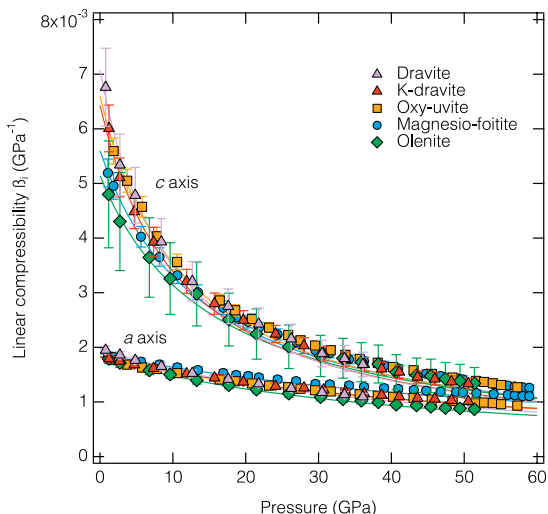[a] Fit done using the data presented in these studies.

FIGURE 4. Linear compressibility of each synthetic tourmaline along the **a** and **c** axes. Symbols represent values determined for synthetic tourmaline in the high-pressure single-crystal X-ray diffraction experiments and the solid curves represent the parametrized fit of a modified third-order Birch-Murnaghan EoS fit to each of the fully weighted data sets. (Color online.)

conditions, consistent with previous findings (see references in Table 1). This behavior is similar to other cyclosilicates (e.g., beryl; Hazen et al. 1986) and is interpreted to reflect the relative incompressibility of the ring structures parallel to **a** (Fig. 1). The presence of the highly compressible X site in the **c** direction further contributes to tourmaline's anisotropic elasticity (O'Bannon et al. 2018). Tourmaline's elastic anisotropy decreases with increasing pressure and the axial compressibilities converge near 60 GPa at which point the **c** axis is only ~14% more compressible than the **a** axis (Fig. 4).

INFLUENCE OF TOURMALINE COMPOSITION ON COMPRESSIBILITY

Primary role of Al content

Al is a key cation in tourmaline, as indicated by it being a defining constituent of 28 out of the 33 end-member species. Consequently, it is a major element in all naturally occurring tourmalines. Al is primarily incorporated at the octahedral sites (Y and Z), with a preference for the network-forming Z site (Bosi 2018). To a lesser extent, it is also incorporated at the T site (Table 2).

The Al content of tourmaline is known to exert a strong influence on the long-range crystal structure, particularly in terms of a negative correlation between Al content and the c unit-cell parameter (Bosi et al. 2010). Interestingly, the Z site composition is more strongly correlated to unit-cell volume than the larger X site (Fig. 2). This likely reflects the importance of the long-range network formed by the coordinated Z sites in both the **a** and **c** directions. Moreover, the formation of 3_1 spiral chains of Z coordination polyhedra along **c** accounts for Al's strong influence on the length of the **c** axis (Fig. 1). In addition, high Al contents have been correlated to increased incorporation of tetrahedral B (^TB) in tourmaline (Ertl et al. 2008a). As a result, ^TB has been observed in natural olenite (e.g., 1 ^TB pfu; Hughes et al. 2000) and is present in significant quantities in the synthetic olenite investigated here (Table 2). Incorporation of B at the T site reduces the average $<T\text{-}O>$ bond length and the corresponding unit-cell volume (Fig. 2; Ertl et al. 2018), albeit not as significantly as the octahedral sites. By encouraging the incorporation of ^TB, Al content strengthens its own influence on the unit-cell volume of tourmaline.

Here, the Mg-free synthetic olenite has both octahedral sites fully occupied by Al, allowing the direct investigation of the effect of Al on tourmaline compressibility compared with Mg-Al tourmalines. The small size of Al relative to other octahedral-site-occupying ions results in synthetic olenite having the smallest Y and Z sites of all the investigated synthetic tourmalines, as well as being smaller than naturally occurring tourmalines (Fig. 2). As expected, the high Al leads to a significant reduction in the unit-cell parameters at all pressures relative to the Mg-Al tourmalines (Fig. 3).

In regards to tourmaline's bulk compressibility, there is no immediately obvious correlation with Al content. The ambient isothermal bulk modulus of olenite is comparable to that of Mg-bearing magnesio-foitite and its pressure derivative to those of the dravitic tourmalines (Table 1). However, when comparing K_0 and K'_0 values, it is important to bear in mind that these parameters co-vary during fitting (Bass et al. 1981; Angel 2000). When the covariance is considered, it becomes evident that the bulk compressibility of the Mg-Al tourmaline (dravite, K-dravite, oxy-uvite, and magnesio-foitite) are correlated, with olenite showing distinctly higher K_0 and K'_0 values (Fig. 5).

The lower bulk compressibility of Al-dominant tourmaline is primarily accounted for by its reduced compressibility along the **c** axis. There is a correlation between the c_0 unit-cell parameter and the ambient linear compressibility of the **c** axis (β_{c0}) (Fig. 6). As the c_0 parameter is sensitive to the Al content

of tourmaline, especially at the Z site, olenite, followed by the most Al-rich of the Mg-Al tourmaline, magnesio-foitite, are the least compressible in the **c**-axis direction. In contrast, no correlation between a_0 and β_{a0} is observed. The influence of the Al content on tourmaline's compressibility especially along **c** is interpreted to reflect the primary control of the 3_1 ZO_6 spiral chains, preferentially occupied by Al. The correlation between linear compressibility along **c** (β_c) and Al content does not persist at high pressure. Instead, β_c values for the different tourmaline compositions converge by 30 GPa.
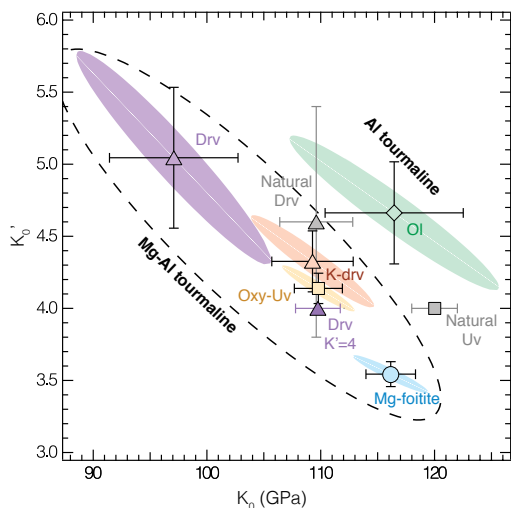
FIGURE 5. Bulk modulus (K_0) and its pressure derivative (K_0') for the synthetic tourmalines (colored symbols) compared to those of natural dravite (O'Bannon et al. 2018) and uvite (Xu et al. 2012). The covariation of K_0 and K_0' in the third-order Birch Murnaghan fit for the synthetic tourmalines is shown as colored ovals behind their respective symbol. (Color online.)
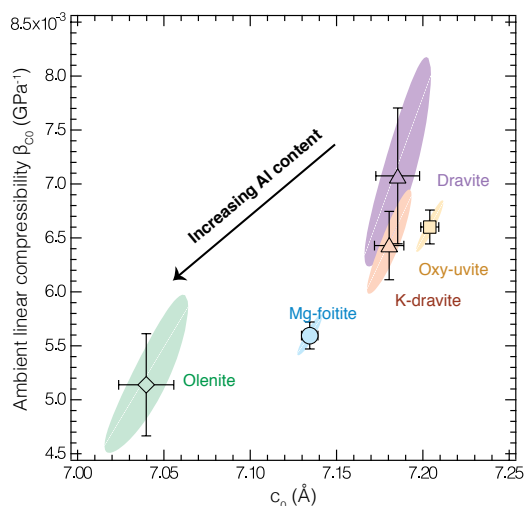

FIGURE 6. Ambient linear compressibility of the **c** axis (β_{c0}) plotted against the respective tourmaline's ambient length (c_0). The covariation of the linear compressibility and the refined c_0 value is shown as a colored oval behind each tourmaline's respective symbol. (Color online.)

Secondary role of *X*-site occupancy

The ninefold-coordinated X site is the largest site in the tourmaline structure and is located directly above the center of the six-membered ring along **c** (Fig. 1). Similar to the role of large cations and water in other ring silicates, the X site has been posited to be responsible for tourmaline's relatively increased compressibility in the **c** direction (Dietrich 1985). Tourmaline exhibits distinctly increased compressibility along **c** in comparison to the cyclosilicates beryl and cordierite, which has been thought to reflect the higher concentration of the highly compressible X site in tourmaline (Xu et al. 2016; O'Bannon et al. 2018). The occupancy and composition of the X site has therefore been previously expected to have a significant influence on tourmaline compressibility.

The Mg-Al tourmalines investigated here (K-dravite, dravite, oxy-uvite, and magnesio-foitite) each have a distinct X-site composition, including all the major X-site occupants of the tourmaline group (K, Na, Ca, and □, respectively). Contrary to expectations, the X site does not exert a primary control on tourmaline compressibility, as K_0 is similar for all the tourmalines. However, the presence of a nearly completely vacant X site in magnesio-foitite is correlated with a lower K_0' value relative to the other tourmalines (Fig. 5). It should be noted that in the third-order P-V EoS, dravite's P-V behavior is fit with a high K_0' value. This may be taken to reflect its low number of X-site vacancies. However, this interpretation is not supported by the K_0' value of K-dravite, which has a similar number of X-site vacancies (Table 2). As shown in the F_E-f plots in the Supplementary Material[1], the second-order P-V EoS fits the dravite data equally well. As a result, we have chosen not to interpret the high K_0' value of dravite's third-order P-V EoS as reflecting a compositional control.

Close inspection of the linear compressibility at high pressure (Fig. 4) suggests that the lower K_0' value of magnesio-foitite results from increased compressibility along **a** (β_a) at high pressure. Compression along **a** is expected to be influenced by compression of the six-membered ring, which lies parallel to **a**. Although the T site has relatively low compressibility, deformation of the six-membered ring it forms plays a central role in tourmaline's behavior under compression (O'Bannon et al. 2018). More specifically, in natural dravite, O'Bannon et al. (2018) show this deformation comprises a continuous increase in ditrigonality of the ring structure combined with crimping and puckering up to ~15 GPa. After the loss of the mirror plane above ~15 GPa, ring deformation was reported to be primarily accommodated by increasing ditrigonality and tetrahedral rotation. Interestingly, it is near this pressure that magnesio-foitite begins displaying increased compressibility along **a** relative to the principally X-site-occupied tourmalines. Magnesio-foitite is known to have a distinct ring morphology characterized by increased crimping, a feature that also affects its electronic structure (Berryman et al. 2016). It is therefore not surprising that magnesio-foitite might exhibit slight differences in the compressive behavior of its ring structure. We can therefore speculate that the presence of a vacant X site is somehow facilitating increased compression along **a** relative to the other Mg-Al tourmalines. However, it is important to note that olenite maintains reduced compressibility along **a** despite having significant X-site vacancies. This observation

underlines the predominant role of Al content and the octahedral sites on the structure's compressibility in all directions.

IMPLICATIONS

The tourmaline supergroup is exceptional in terms of its chemical flexibility. The presence of three-, four-, six-, and ninefold-coordinated sites in its structure allows it to incorporate a range of cations of varying size and charge. This apparent divergence from Pauling's rule of parsimony might be expected to reduce tourmaline's stability (Bosi 2018). Despite this, tourmaline is observed to be stable throughout the crust (van Hinsberg et al. 2011) and potentially in the uppermost mantle (Marschall et al. 2009). Under static compression at room temperature, none of the five investigated synthetic tourmalines shows any indication of a reconstructive phase transition or amorphization up to 60 GPa, revealing the remarkable metastability of this complex structure. However, the possibility of an undetected subtle phase transition cannot be ruled out as O'Bannon et al. (2018) reported a second-order phase transition in dravitic tourmaline from rhombohedral $R3m$ to rhombohedral $R3$ at ~15.4 GPa. Tourmaline maintains its topology through this transition, and the high-pressure phase differs from the lower-pressure structure only by the absence of the mirror plane.

Tourmaline's metastability to high pressure exists in sharp contrast to the behavior of other cyclosilicates. Cordierite undergoes two reconstructive first-order phase transitions characterized by increasing amounts of polymerization of Si by 15.4 GPa at room temperature (Finkelstein et al. 2015). Beryl, another cyclosilicate of interest, is observed to be stable to at least 9.5 GPa in high-pressure XRD experiments (Fan et al. 2015), but ab initio calculations and high-pressure spectroscopic data indicate a displacive phase transition is expected at 14 GPa (Prencipe et al. 2011; O'Bannon and Williams 2016). These cyclosilicates differ from tourmaline by the presence of open channels formed by the alignment of the six-membered rings within their long-range structure. In contrast, the polar six-membered rings in tourmaline are separated by the presence of three corner-sharing Y-site octahedra as well as the ninefold-coordinated X site. Tourmaline's structure is additionally differentiated from other cyclosilicates by its framework of Z-site octahedra that extend in the **a** and **c** directions. It is important to note that X-site-vacant magnesio-foitite exhibits the same level of metastability as the X-site-occupied tourmalines. Moreover, magnesio-foitite exhibits generally similar compressibility, including anisotropic compressibility, as the other tourmalines. This comparison not only indicates that the X-site-occupying ion does not have a strong influence on tourmaline's compressibility, but that it is also not pivotal in the stability of the tourmaline structure. Our results instead forward the hypothesis that the chemically flexible octahedral Y and Z sites are primarily responsible for the mechanical flexibility and extensive (meta)stability of the tourmaline structure.

Tourmaline's extensive chemical flexibility and high-pressure, room-temperature behavior is therefore perhaps more comparable to that of the clinopyroxenes and amphiboles than it is to the cyclosilicates. Grunerite amphibole is metastable to at least 25 GPa (Yong et al. 2018) and clinopyroxene does not exhibit a reconstructive phase transition until 50 GPa (Plonka et al. 2012). Moreover, the two displacive phase transitions recorded in clinopyroxenes and amphiboles are due to the kinking of the chains of tetrahedra (Welch et al. 2007; Yong et al. 2018). This behavior is interestingly analogous to the behavior of tourmaline's six-membered ring under compression. During compression, the ring structure in dravite is reported by O'Bannon et al. (2018) to exhibit increasing ditrigonality and puckering.

Synthetic crystals provide critical insight into the role of composition on tourmaline's properties. They are especially useful for characterizing the effect of end-member components that are common, but rarely dominant in natural tourmaline, such as magnesio-foitite and olenite. Questions concerning the effect of particular components on tourmaline's properties in tourmaline can thus unambiguously be explored without having to survey a wide range of chemically complex natural tourmaline compositions. Here, a comparison of the Mg-Al tourmalines (dravite, K-dravite, magnesio-foitite, and oxy-uvite) to a pure Al-tourmaline (olenite) revealed the primary role of Al on tourmaline's compressibility. In addition, comparison of a completely X-site-vacant tourmaline (magnesio-foitite) to the nominally X-site-occupied tourmalines revealed the secondary role of X-site-occupancy on compressibility along **a**. Substitution of Na, Ca, and K does not have a demonstrable effect on compressibility. Moreover, a comparison of the different tourmalines demonstrates that the X site is not responsible for tourmaline's extensive (meta)stability.

As well as exerting a dominant control on tourmaline's compressibility and its unit-cell parameters, the octahedral Y and Z sites show the largest degree of compositional variability. In the tourmaline investigated here, these sites were solely occupied by Mg and Al, or in the case of olenite, only Al. However, these sites can also be occupied by Li^+, Fe^{2+}, Fe^{3+}, Mn^{2+}, Cr^{3+}, and V^{3+} as major constituents, or by Ni^{2+}, Co^{2+}, Cu^{2+}, Zn^{2+}, Ga^{3+}, Mn^{3+}, and Ti^{4+} as minor constituents in natural tourmaline (Bosi 2018). The varying size and charge of these ions, particularly those occurring at the network-forming Z site, may have a minor effect on tourmaline's compressibility. A significant povondraite $[NaFe_3^{3+}(Fe_4^{3+}Mg_2)Si_6O_{18}(BO_3)_3(OH)_3O]$ component will significantly expand tourmaline's unit-cell volume (Fig. 2) relative to Mg-Al tourmaline. It is therefore expected that tourmaline with a large povondraite component may show increased compressibility along **c** and correspondingly smaller K_0, an effect that would oppose the stiffening effect of Al.

As the major host of B in the crust, the inclusion of tourmaline in geochemical models is vital to developing an understanding of the B cycle. However, thermodynamic data for tourmaline is lacking (van Hinsberg and Schumacher 2007). The presented isothermal bulk moduli and their pressure derivatives for synthetic tourmalines provide essential compressibility data for natural Mg-Al tourmalines. These parameters are especially important for volume-sensitive reactions common to environments of mass transfer. The results motivate the need for additional compressibility studies on other near-end-member tourmalines, especially povondraite, as well as the use of synthetic crystals in constraining other thermodynamic parameters, such as thermal expansivities.

REFERENCES CITED

Angel, R.J. (2000) Equations of state. In R.M. Hazen and R.T. Downs, Eds., High-temperature and high-pressure crystal chemistry. Reviews in Mineralogy, 41, 35–60.

Angel, R.J., Gonzalez-Platas, J., and Alvaro, M. (2014) EosFit7c and a Fortran module (library) for equation of state calculations. Zeitschrift für Kristallographie, 229, 405–419.

Bačík, P., Cempírek, J., Uher, P., Novák, M., Ozdín, D., Filip, J., Škoda, R., Breiter, K., Klementová, M., and Ďuďa, R. (2013) Oxy-schorl, $Na(Fe_2^{2+}Al)Al_6Si_6O_{18}(BO_3)_3(OH)_3O$, a new mineral from Zlatá Idka, Slovak Republic and Přibyslavice, Czech Republic. American Mineralogist, 98, 485–492.

Bačík, P., Ertl, A., Števko, M., Giester, G., and Sečkár, P. (2015) Acicular zoned tourmaline (magnesio-foitite to foitite) from a quartz vein near Tisovec, Slovakia: the relationship between crystal chemistry and acicular habit. Canadian Mineralogist, 53, 221–234.

Bass, J.D., Liebermann, R.C., Weidner, D.J., and Finch, S.J. (1981) Elastic properties from acoustic and volume compression experiments. Physics of the Earth and Planetary Interiors, 25, 140–158.

Berryman, E., Wunder, B., and Rhede, D. (2014) Synthesis of K-dominant tourmaline. American Mineralogist, 99, 539–542.

Berryman, E.J., Wunder, B., Wirth, R., Rhede, D., Schettler, G., Franz, G., and Heinrich, W. (2015) An experimental study on K and Na incorporation in dravitic tourmaline and insight into the origin of diamondiferous tourmaline from the Kokchetav Massif, Kazakhstan. Contributions to Mineralogy and Petrology, 169, 28.

Berryman, E.J., Wunder, B., Rhede, D., Schettler, G., Franz, G., and Heinrich, W. (2016a) P-T-X controls on Ca and Na partition between Mg-Al tourmaline and fluid. Contributions to Mineralogy and Petrology, 171, 31.

Berryman, E.J., Wunder, B., Ertl, A., Koch-Müller, M., Rhede, D., Scheidl, K., Giester, G., and Heinrich, W. (2016b) Influence of the X-site composition on tourmaline's crystal structure: investigation of synthetic K-dravite, dravite, oxy-uvite, and magnesio-foitite using SREF and Raman spectroscopy. Physics and Chemistry of Minerals, 43, 83–102.

Boffa Ballaran, T., Kurnosov, A., Glazyrin, K., Frost, D.J., Merlini, M., Hanfland, M., and Caracas, R. (2012) Effect of chemistry on the compressibility of silicate perovskite in the lower mantle. Earth and Planetary Science Letters, 333-334, 181–190.

Bosi, F. (2008) Disordering of Fe^{2+} over octahedrally coordinated sites of tourmaline. American Mineralogist, 93, 1647–1653.

——— (2018) Tourmaline crystal chemistry. American Mineralogist, 103, 298–306.

Bosi, F., and Lucchesi, S. (2007) Crystal chemical relationships in the tourmaline group: structural constraints on chemical variability. American Mineralogist, 92, 1054–1063.

Bosi, F., Balić-Žunić, T., and Surour, A.A. (2010) Crystal structure analyses of four tourmaline specimens from the Cleopatra's Mines (Egypt) and Jabal Zalm (Saudi Arabia), and the role of Al in the tourmaline group. American Mineralogist, 95, 510–518.

Bosi, F., Reznitskii, L., and Skogby, H. (2012) Oxy-chromium-dravite, $NaCr_3(Cr_4Mg_2)(Si_6O_{18})(BO_3)_3(OH)_3O$, a new mineral species of the tourmaline supergroup. American Mineralogist, 97, 2024–2030.

Bosi, F., Andreozzi, G.B., Skogby, H., Lussier, A.J., Abdu, Y., and Hawthorne, F.C. (2013a) Fluor-elbaite, $Na(Li_{1.5}Al_{1.5})Al_6(Si_6O_{18})(BO_3)_3(OH)_3F$, a new mineral species of the tourmaline supergroup. American Mineralogist, 98, 297–303.

Bosi, F., Reznitskii, L., and Sklyarov, E.V. (2013b) Oxy-vanadium-dravite, $NaV_3(V_4Mg_2)(Si_6O_{18})(BO_3)_3(OH)_3O$: crystal structure and redefinition of the "vanadium-dravite" tourmaline. American Mineralogist, 98, 501–505.

Bosi, F., Skogby, H., Hålenius, U., and Reznitskii, L. (2013c) Crystallographic and spectroscopic characterization of Fe-bearing chromo-alumino-povondraite and its relations with oxy-chromium-dravite and oxy-dravite. American Mineralogist, 98, 1557–1564.

Bosi, F., Reznitskii, L., Skogby, H., and Hålenius, U. (2014a) Vanadio-oxy-chro-

mium-dravite, $NaV_3(Cr_4Mg_2)(Si_6O_{18})(BO_3)_3(OH)_3O$, a new mineral species of the tourmaline supergroup. American Mineralogist, 99, 1155–1162.

Bosi, F., Skogby, H., Reznitskii, L., and Hålenius, U. (2014b) Vanadio-oxy-dravite, $NaV_3(Al_4Mg_2)(Si_6O_{18})(BO_3)_3(OH)_3O$, a new mineral species of the tourmaline supergroup. American Mineralogist, 99, 218–224.

Bosi, F., Andreozzi, G.B., Hålenius, U., and Skogby, H. (2015a) Experimental evidence for partial Fe^{2+} disorder at the Y and Z sites of tourmaline: a combined EMP, SREF, MS, IR and OAS study of schorl. Mineralogical Magazine, 79, 515–528.

Bosi, F., Andreozzi, G.B., Agrosì, G., and Scandale, E. (2015b) Fluor-tsilaisite, $NaMn_3Al_6(Si_6O_{18})(BO_3)_3(OH)_3F$, a new tourmaline from San Piero in Campo (Elba, Italy) and new data on tsilaisitic tourmaline from the holotype specimen locality. Mineralogical Magazine, 79, 89–101.

Bosi, F., Skogby, H., Lazor, P., and Reznitskii, L. (2015c) Atomic arrangements around the O3 site in Al- and Cr-rich oxy-tourmalines: a combined EMP, SREF, FTIR and Raman study. Physics and Chemistry of Minerals, 42, 441–453.

Bosi, F., Skogby, H., and Hålenius, U. (2016a) Thermally induced cation redistribution in Fe-bearing oxy-dravite and potential geothermometric implications. Contributions to Mineralogy and Petrology, 171, 47.

Bosi, F., Skogby, H., and Balić-Žunić, T. (2016b) Thermal stability of extended clusters in dravite: a combined EMP, SREF and FTIR study. Physics and Chemistry of Minerals, 43, 395–407.

Bosi, F., Reznitskii, L., Hålenius, U., and Skogby, H. (2017a) Crystal chemistry of Al-V-Cr oxy-tourmalines from Sludyanka complex, Lake Baikal, Russia. European Journal of Mineralogy, 29, 457–472.

Bosi, F., Cámara, F., Ciriotti, M.E., Hålenius, U., Reznitskii, L., and Stagno, V. (2017b) Crystal-chemical relations and classification problems of tourmalines belonging to the oxy-schorl–oxy-dravite–bosiite–povondraite series. European Journal of Mineralogy, 29, 445–455.

Cempírek, J., Houzar, S., Novák, M., Groat, L.A., Selway, J.B., and Šrein, V. (2013) Crystal structure and compositional evolution of vanadium-rich oxy-dravite from graphite quartzite at Bítovánky, Czech Republic. Journal of Geosciences, 58, 149–162.

Clark, C.M., Hawthorne, F.C., and Ottolini, L. (2011) Fluor-dravite, $NaMg_3Al_6Si_6O_{18}(BO_3)_3(OH)_3F$, a new mineral species of the tourmaline group from the Crabtree emerald mine, Mitchell County, North Carolina: description and crystal structure. Canadian Mineralogist, 49, 57–62.

Clemens, P., and Prakapenka, V.B. (2015) DIOPTAS: a program for reduction of two-dimensional X-ray diffraction data and data exploration. High Pressure Research, 35, 223–230.

Dera, P., Zhuravlev, K., Prakapenka, V., Rivers, M.L., Finkelstein, G.J., Grubor-Urosevic, O., Tschauner, O., Clark, S.M., and Downs, R.T. (2013) High pressure single-crystal micro X-ray diffraction analysis with GSE_ADA/RSV software. High Pressure Research, 33, 466–484.

Dewaele, A., Loubeyre, P., and Mezouar, M. (2004) Equations of state of six metals above 94 GPa. Physical Review B, 70, 094112.

Dietrich R.V. (1985) The Tourmaline Group. Van Nostrand Reinhold Company, New York, 300 p.

Dutrow, B.L., and Henry, D.J. (2011) Tourmaline: A Geologic DVD. Elements, 7, 301–306.

Ertl, A., Hughes, J.M., Prowatke, S., Rossman, G.R., London, D., and Fritz, E.A. (2003) Mn-rich tourmaline from Austria: structure, chemistry, optical spectra, and relations to synthetic sold solutions. American Mineralogist, 88, 1369–1376.

Ertl, A., Kolitsch, U., Prowatke, S., Dyar, M.D., and Henry, D.J. (2006) The F-analog of schorl from Grasstein, Trentino–South Tyrol, Italy: crystal structure and chemistry. European Journal of Mineralogy, 18, 583–588.

Ertl, A., Hughes, J.M., Prowatke, S., Ludwig, T., Brandstätter, F., Körner, W., and Dyar, M.D. (2007) Tetrahedrally-coordinated boron in Li-bearing olenite from "mushroom" tourmaline from Momeik, Myanmar: structure and chemistry. Canadian Mineralogist, 45, 891–899.

Ertl, A., Tillmanns, E., Ntaflos, T., Francis, C., Giester, G., Körner, W., Hughes, J.M., Lengauer, C., and Prem, M. (2008a) Tetrahedrally coordinated boron in Al-rich tourmaline and its relationship to the pressure-temperature conditions of formation. European Journal of Mineralogy, 20, 881–888.

Ertl, A., Rossman, G.R., Hughes, J.M., Ma, C., and Brandstätter, F. (2008b) V^{3+}-bearing, Mg-rich, strongly disordered olenite from a graphite deposit near Amstall, Lower Austria: A structural, chemical and spectroscopic investigation. Neues Jahrbuch für Mineralogie Abhandlungen, 184, 243–253.

Ertl, A., Kolitsch, U., Meyer, H.-P., Ludwig, T., Lengauer, C.L., Nasdala, L., and Tillmanns, E. (2009) Substitution mechanism in tourmalines of the "fluor-elbaite"-rossmanite series from Wolkenburg, Saxony, Germany. Neues Jahrbuch für Mineralogie Abhandlungen, 186, 51–61.

Ertl, A., Rossman, G.R., Hughes, J.M., London, D., Wang, Y., O'Leary, J.A., Dyar, M.D., Prowatke, S., Ludwig, T., and Tillmanns, E. (2010a) Tourmaline of the elbaite-schorl series from the Himalaya Mine, Mesa Grande, California, U.S.A.: A detailed investigation. American Mineralogist, 95, 24–40.

Ertl, A., Marschall, H.R., Giester, G., Henry, D.J., Schertl, H.-P., Ntaflos, T., Luvizotto, G.L., Nasdala, L., and Tillmanns, E. (2010b) Metamorphic ultra

high-pressure tourmalines: Structure, chemistry, and correlations to PT conditions. American Mineralogist, 95, 1–10.

Ertl, A., Mali, H., Schuster, R., Körner, W., Hughes, J.M., Brandstätter, F., and Tillmanns, E. (2010c) Li-bearing, disordered Mg-rich tourmalines from the pegmatite-marble contact from the Austroalpine basement units (Styria, Austria). Mineralogy and Petrology, 99, 89–104.

Ertl, A., Giester, G., Ludwig, T., Meyer, H.P., and Rossman, G.R. (2012a) Synthetic B-rich olenite: Correlations of single-crystal structural data. American Mineralogist, 97, 1591–1597.

Ertl, A., Schuster, R., Hughes, J.M., Ludwig, T., Meyer, H.-P., Finger, F., Dyar, M.D., Ruschel, K., Rossman, G.R., Klötzi, U., and others. (2012b) Li-bearing tourmalines in Variscan granitic pegmatites from the Moldanubian nappes, Lower Austria. European Journal of Mineralogy, 24, 695–715.

Ertl, A., Kolitsch, U., Dyar, M.D., Hughes, J.M., Rossman, G.R., Pieczka, A., Henry, D.J., Pezzotta, F., Prowatke, S., Lengauer, C.L., and others. (2012c) Limitations of Fe^{2+}- and Mn^{2+}-rich and Mn^{2+} site occupancy in tourmaline: evidence from Fe^{2+} tourmaline. American Mineralogist, 97, 1402–1416.

Ertl, A., Giester, G., Schüssler, U., Brätz, H., Okrusch, M., Tillmanns, E., and Bank, H. (2013) Cu- and Mn-bearing tourmalines from Brazil and Mozambique: Crystal structures, chemistry and correlations. Mineralogy and Petrology, 107, 265–279.

Ertl, A., Baksheev, I.A., Giester, G., Lengauer, C.L., Prokofiev, V.Y., and Zorina, L.D. (2016a) Bosiite, $NaFe_3^{3+}(Al_4Mg_2)(Si_6O_{18})(BO_3)_3(OH)_3O$, a new ferric member of the tourmaline supergroup from the Darasun gold deposit, Transbaikalia, Russia. European Journal of Mineralogy, 28, 581–591.

Ertl, A., Kolitsch, U., Dyar, M.D., Meyer, H.-P., Henry, D.J., Rossman, G.R., Prem, M., Ludwig, T., Nasdala, L., Lengauer, C.L., and others. (2016b) Fluor-schorl, a new member of the tourmaline supergroup, and new data on schorl from the cotype localities. European Journal of Mineralogy, 28, 163–177.

Ertl, A., Henry, D.J., and Tillmanns, E. (2018) Tetrahedral substitutions in tourmaline: a review. European Journal of Mineralogy, 30, 465–470.

Fan, D., Xu, J., Kuang, Y., Li, X., Li, Y., and Xie, H. (2015) Compressibility and equation of state of beryl ($Be_3Al_2Si_6O_{18}$) by using a diamond anvil cell and in situ synchrotron X-ray diffraction. Physics and Chemistry of Minerals, 42, 529–539.

Fei, Y., Ricolleau, A., Frank, M., Mibe, K., Shen, G., and Prakapenka, V. (2007) Toward an internally consistent pressure scale. Proceedings of National Academy of Sciences, 104, 9182–9186.

Filip, J., Bosi, F., Novák, M., Skogby, H., Tuček, J., Čuda, J., and Wildner, M. (2012) Redox processes of iron in the tourmaline structure: Example of the high-temperature treatment of Fe^{3+}-rich schorl. Geochimica et Cosmochimica Acta, 86, 239–256.

Finger, L.W., Hazen, R.M., Zou, G., Mao, H.K., and Bell, P.M. (1981) Structure and compression of crystalline argon and neon at high pressure and room temperature. Applied Physics Letters, 39, 892–894.

Finkelstein, G.J., Dera, P.K., and Duffy, T.S. (2015) High-pressure phases of cordierite from single-crystal X-ray diffraction to 15 GPa. American Mineralogist, 100, 1821–1833.

Gatta, G.D., Danisi, R.M., Adamo, I., Meven, M., and Diella, V. (2012) A single-crystal neutron and X-ray diffraction study of elbaite. Physics and Chemistry of Minerals, 39, 577–588.

Gonzalez-Platas, J., Alvaro, M., Nestola, F., and Angel, R. (2016) EosFit7-GUI: a new graphical user interface for equation of state calculations, analyses and teaching. Journal of Applied Crystallography, 49, 1377–1382.

Grew, E.S., Bosi, F., Gunter, M., Hålenius, U., Trumbull, R.B., and Yates, M.G. (2018) Fluor-elbaite, lepidolite and Ta-Nb oxides from a pegmatite of the 3000 Ma Sinceni pluton, Swaziland: Evidence for lithium-cesium-tantalum (LCT) pegmatites in the Mesoarchean. European Journal of Mineralogy, 30, 205–218.

Grice, J.D., Ercit, T.S., and Hawthorne, F.C. (1993) Povondraite, a redefinition of the tourmaline ferridravite. American Mineralogist, 78, 433–436.

Hazen, R.M., Au, A.Y., and Finger, L.W. (1986) High-pressure crystal chemistry of beryl ($Be_3Al_2Si_6O_{18}$) and euclase ($BeAlSiO_4OH$). American Mineralogist, 71, 977–984.

Helme, B.G., and King, P.J. (1978) The elastic constants of iron tourmaline (schörl). Journal of Materials Science, 13, 1487–1489.

Hemingway, B.S., Evans, H.T. Jr., Mazdab, F.K., and Anovitz, L.M. (1996) Thermal expansion of some borate and borosilicate minerals (fluoborite, danburite, sinhalite, datolite, elbaite, dravite, kornerupine, dumortierite, ferro-axinite, and manganaxinite) between 25 and about 1200°C. U.S. Geological Survey, Open File Report 96-100.

Henry, D.J., and Dutrow, B.L. (1992) Tourmaline in low grade clastic metasedimentary rock: an example of the petrogenetic potential of tourmaline. Contributions to Mineralogy and Petrology, 112, 203–218.

——— (1996) Metamorphic tourmaline. In E.S. Grew and L.M. Anovitz, Eds., Boron: mineralogy, petrology and geochemistry in the earth's crust. Reviews in Mineralogy, 33, 500–555.

Henry, D.J., and Guidotti, C.V. (1985) Tourmaline as a petrogenetic indicator mineral: an example from the staurolite-grade metapelites of NW Maine. American Mineralogist, 70, 1–15.

Henry, D.J., Novák, M., Hawthorne, F.C., Ertl, A., Dutrow, B.L., Uher,P., and Pezzotta, F. (2011) Nomenclature of the tourmaline-supergroup minerals. American Mineralogist, 96, 895–913.

Hughes, J.M., Ertl, A., Dyar, M.D., Grew, E.S., Shearer, C.K., Yates, M.G., and Guidotti, C.V. (2000) Tetrahedrally coordinated boron in a tourmaline: boron-rich olenite from Stoffhütte, Koralpe, Austria. Canadian Mineralogist, 38, 861–868.

Hughes, K.-A., Hughes, J.M., and Dyar, M.D. (2001) Chemical and structural evidence for [4]B↔[4]Si substitution in natural tourmalines. European Journal of Mineralogy, 13, 743–747.

Krosse, S. (1995) Hochdrucksynthese, Stabilität und Eigenschaften der Borsilikate Dravit und Kornerupin sowie Darstellung und Stabilitätsverhalten eines neuen Mg–Al-borates. Dr. rer. nat. thesis, Ruhr-Universität Bochum.

Kutzschbach, M., Wunder, B., Rhede, D., Koch-Müller, M., Ertl, A., Giester, G., Heinrich, W., and Franz, G. (2016) Tetrahedral boron in natural and synthetic HP/UHP tourmaline: Evidence from Raman spectroscopy, EMPA, and single-crystal XRD. American Mineralogist, 101, 93–104.

Kutzschbach, M., Wunder, B., Trumbull, R.B., Rocholl, A., Meixner, A., and Heinrich, W. (2017) An experimental approach to quantify the effect of tetrahedral boron in tourmaline on the boron isotope fractionation between tourmaline and fluid. American Mineralogist, 102, 2505–2511.

Larson, A.C., and von Dreele, R.B. (1987) Generalized structure analysis system. Los Alamos National Laboratory Report LAUR 86-748.

Li, H., Qin, S., Zhu, X., Liu, J., Li, X., Wu, X., and Wu, Z. (2004) In situ high-pressure X-ray diffraction of natural tourmaline. Nuclear Techniques, 27, 919–922. (In Chinese.)

London, D., Ertl, A., Hughes, J.M., Morgan, G.B. VI, Fritz, E.A., and Harms, B.S. (2006) Synthetic Ag-rich tourmaline: structure and chemistry. American Mineralogist, 91, 680–684.

Lussier, A.J., Aguiar, P.M., Michaelis, V.K., Kroeker, S., Herwig, S., Abdu, Y., and Hawthorne, F.C. (2008) Mushroom elbaite from the Kat Chay mine, Momeik, near Mogok, Myanmar: I. Crystal chemistry by SREF, EMPA, MAS NMR and Mössbauer spectroscopy. Mineralogical Magazine, 72, 747–761.

Lussier, A.J., Hawthorne, F.C., Abdu, Y., Herwig, S., Michaelis, V.K., Aguiar, P.M., and Kroeker, S. (2011a) The crystal chemistry of "wheatsheaf" tourmaline from Mogok, Myanmar. Mineralogical Magazine, 72, 999–1010.

Lussier, A.J., Abdu, Y. Hawthorne, F.C., Michaelis, V.K., Aguiar, P.M., and Kroeker, S. (2011b) Oscillatory zoned liddicoatite from Anjanabonoina, central Madagascar. I. Crystal chemistry and structure by SREF and ^{11}B and ^{27}Al MAS NMR spectroscopy. Canadian Mineralogist, 49, 63–88.

Lussier, A., Ball, N.A., Hawthorne, F.C., Henry, D.J., Shimizu, R., Ogasawara, Y., and Ota, T. (2016) Maruyamaite, $K(MgAl_2)(Al_5Mg)Si_6O_{18}(BO_3)_3(OH)_3O$, a potassium-dominant tourmaline from the ultrahigh-pressure Kokchetav massif, northern Kazakhstan: description and crystal structure. American Mineralogist, 101, 355–361.

Marler, B., Borowski, M., Wodara, U., and Schreyer, W. (2002) Synthetic tourmaline (olenite) with excess boron replacing silicon in the tetrahedral site: II. Structural analysis. European Journal of Mineralogy, 14, 763–771.

Marschall, H.R., Ertl, A., Hughes, J.M., and McCommon, C. (2004) Metamorphic Na- and OH-rich disordered dravite with tetrahedral boron associated with omphacite, from Syros, Greece: Chemistry and structure. European Journal of Mineralogy, 16, 817–823.

Marschall, H.R., Korsakov, A.V., Luvizotto, G.L., Nasdala, L., and Ludwig, T. (2009) On the occurrence and boron isotopic composition of tourmaline in (ultra)high-pressure metamorphic rocks. Journal of the Geological Society, London, 166, 811–823.

Novák, M., Ertl, A., Povondra, P., Galiová, M.V., Rossman, G.R., Pristacz, H., Prem, M., Giester, G., Gadas, P., and Škoda, R. (2013) Darrellhenryite, $Na(LiAl_2)Al_6(BO_3)_3Si_6O_{18}(OH)_3O$, a new mineral from the tourmaline supergroup. American Mineralogist, 98, 1886–1892.

O'Bannon, E. III and Williams, Q. (2016) Beryl-II, a high-pressure phase of beryl: Raman and luminescence spectroscopy to 16.4 GPa. Physics and Chemistry of Minerals, 43, 671–687.

O'Bannon, E. III, Beavers, C.M., Kunz, M., and Williams, Q. (2018) High-pressure study of dravite tourmaline: Insights into the accommodating nature of the tourmaline structure. American Mineralogist, 103, 1622–1633.

Ogorodova, L.P., Melchakova, L.V., Kiseleva, I.A., and Peretyazhko, I.S. (2004) Thermodynamics of natural tourmaline-elbaite. Thermochimica Acta, 419, 211–214.

Ota, T., Kobayashi, K., Katsura, T., and Nakamura, E. (2008) Tourmaline breakdown in a pelitic system: implications for boron cycling through subduction zones. Contributions to Mineralogy and Petrology, 155, 19–32.

Pandey, C.S., and Schreuer, J. (2012) Elastic and piezoelectric constants of tourmaline single crystals at non-ambient temperatures determined by resonant ultrasound spectroscopy. Journal of Applied Physics, 111, 013516.

Plonka, A., Dera, P., Irmen, P., Rivers, M.L., Ehm, L., and Parise, J.B. (2012) β-diopside, a new ultrahigh-pressure polymorph of $CaMgSi_2O_6$ with six-coordinated silicon. Geophysical Research Letters, 39, L24307.

Prencipe, M., Scanavino, I., Nestola, F., Merlini, M., Civalleri, B., Bruno, M.,

and Dovesi, R. (2011) High-pressure thermo-elastic properties of beryl ($Al_4Be_6Si_{12}O_{36}$) from ab initio calculations, and observations about the source of thermal expansion. Physics and Chemistry of Minerals, 38, 223–239.

Reznitskii, L., Clark, C.M., Hawthorne, F.C., Grice, J.D., Skogby, H., Hålenius, U., and Bosi, F. (2014) Chromo-alumino-povondraite, $NaCr_3(Al_4Mg_2)(Si_6O_{18})$ $(BO_3)_3(OH)_3O$, a new mineral species of the tourmaline supergroup. American Mineralogist, 99, 1767–1773.

Rivers, M., Prakapenka, V.B., Kubo, A., Pullins, C., Holl, C.M., and Jacobsen, S.D. (2008) The COMPRES/GSECARS gas-loading system for diamond anvil cells at the Advanced Photon Source. High Pressure Research, 28, 273–292.

Schreyer, W., Wodara, U., Marler, B., van Aken, P., Seifert, F., and Robert, J.-L. (2000) Synthetic tourmaline (olenite) with excess boron replacing silicon on the tetrahedral site: I. Synthesis conditions, chemical and spectroscopic evidence. European Journal of Mineralogy, 12, 529–541.

Schreyer, W., Hughes, J.M., Bernhardt, H.-J., Kalt, A., Prowatke, S., and Ertl, A. (2002) Reexamination of olenite from the type locality: Detection of boron in tetrahedral coordination. European Journal of Mineralogy, 14, 935–942.

Setkova, T.V., Shapovalov, Y.B., and Balitskii, V.S. (2009) Experimental growth and structural-morphological characteristics of Co-tourmaline. Doklady Earth Sciences, 424, 82–85.

Setkova, T.V., Balitsky, V.S., Vereschagin, O.S., and Shapovalov, Y.B. (2017) Hydrothermal synthesis and morphology of Ga-bearing tourmaline. Doklady Earth Sciences, 473, 419–422.

Shimizu, R., and Ogasawara, Y. (2005) Discovery of K-tourmaline in diamond-bearing quartz-rich rock from the Kokchetav Massif, Kazakhstan. Mitteilungen der Österreichischen Mineralogischen Gesellschaft, 150, 141.

Singh, A.K., and Kenichi, T. (2001) Measurement and analysis of nonhydrostatic lattice strain component in niobium to 145 GPa under various fluid pressure-transmitting media. Journal of Applied Physics, 90, 3269–3275.

Tagg, S.L., Cho, H., Dyar, M.D., and Grew, E.S. (1999) Tetrahedral boron in naturally occurring tourmaline. American Mineralogist, 84, 1451–1455.

Tatli, A., and Özkan, H. (1987) Variation of the elastic constants of tourmaline with chemical composition. Physics and Chemistry of Minerals, 14, 172–176.

Tsuchiya, T., and Kawamura, K. (2002) Ab initio study of pressure effect on elastic properties of crystalline Au. The Journal of Chemical Physics, 116, 2121–2124.

van Hinsberg, V.J., and Schumacher, J.C. (2007) Using estimated thermodynamic properties to model accessory phases: the case of tourmaline. Journal of Metamorphic Geology, 25, 769–779.

van Hinsberg, V.J., Henry, D.J., and Marschall, H.R. (2011) Tourmaline: an ideal indicator of its host environment. Canadian Mineralogist, 49, 1–16.

von Goerne, G., Franz, G., and van Hinsberg, V.J. (2011) Experimental determination of Na-Ca distribution between tourmaline and fluid in the system $CaO-Na_2O-MgO-Al_2O_3-SiO_2-B_2O_3-H_2O$. Canadian Mineralogist, 49, 137–152.

Welch, M.D., Cámara, F., Della Ventura, G., and Iezzi, G. (2007) Non-ambient in situ studies of amphiboles. Reviews in Mineralogy and Geochemistry, 67, 223–260.

Wunder, B., Berryman, E., Plessen, B., Rhede, D., Koch-Müller, M., and Heinrich, W. (2015) Synthetic and natural ammonium-bearing tourmaline. American Mineralogist, 100, 250–256.

Xia, X., Weidner, D.J., and Zhao, H. (1998) Equation of state of brucite: single-crystal Brillouin spectroscopy study and polycrystalline pressure-volume-temperature measurement. American Mineralogist, 83, 68–74.

Xu, J., Kuang, Y., Zhang, B., Liu, Y., Fan, D., Li, X., and Xie, H. (2016) Thermal equation of state of natural tourmaline at high pressure and temperature. Physics and Chemistry of Minerals, 43, 315–326.

Xu, J., Zhang, D., Fan, D., Dera, P., Shi, F., and Zhou, W. (2019) Thermoelastic properties of eclogitic garnets and omphacites: implications for deep subduction of oceanic crust and density anomalies in the upper mantle. Geophysical Research Letters, 46, 179−188. DOI:10.1029/2018GL081170.

Yong, T., Dera, P., and Zhang, D. (2018) Single-crystal X-ray diffraction of grunerite up to 25.6 GPa: a high-pressure clinoamphibole polymorph. Physics and Chemistry of Minerals, 46, 215−227. DOI:10.1007/s00269-018-0999-1.

Zhang, L. (1998) Single crystal hydrostatic compression of $(Mg, Mn, Fe, Co)_2SiO_4$ olivines. Physics and Chemistry of Minerals, 25, 308–312.

Zhang, L., Ahsbahs, H., Kutoglu, A., and Geiger, C.A. (1999) Single-crystal hydrostatic compression of synthetic pyrope, almandine, spessartine, grossular and andradite garnets at high pressures. Physics and Chemistry of Minerals, 27, 52–58.

Endnote:

[1]Deposit item AM-19-76967, Supplemental Material. Deposit items are free to all readers and found on the MSA website, via the specific issue's Table of Contents (go to http://www.minsocam.org/MSA/AmMin/TOC/2019/Jul2019_data/Jul2019_data.html).